Available online at www.sciencedirect.com
SCIENCE DIRECT®
PERGAMON
International Journal of Heat and Mass Transfer 46 (2003) 4899–4909
International Journal of HEAT and MASS TRANSFER
www.elsevier.com/locate/ijhmt

Theoretical and numerical analysis of convective heat transfer in the rotating helical pipes

Huajun Chen *, Benzhao Zhang, Jianfeng Ma

Department of Mechanics, Zhejiang University, Hangzhou 310027, PR China

Received 2 October 2002; received in revised form 12 March 2003

Abstract

In terms of the tensor analysis technique, the relative N–S equations and the energy equation in a rotating helical coordinate system are presented in this paper. Convective heat transfer in the rotating helical pipes with circular cross-section is investigated employing theoretical and numerical method. A perturbation solution up to the secondary order is obtained for a small Dean number. Variations of the temperature distribution with the force ratio (the ratio of the Coriolis force to the centrifugal force), the curvature and the torsion are discussed in detail. Present studies also show the natures of the Nusselt number, as well as the effects of the force ratio, the curvature, and the torsion. This study explores many new characteristics of convective heat transfer in the rotating helical pipes and covers wide ranges of parameters.
© 2003 Elsevier Ltd. All rights reserved.

Keywords: Convective heat transfer; Helical pipes; Rotation; Perturbation method; Numerical simulation

1. Introduction

Since the initial work by Dean [1,2], the flow and heat transfer through a curved duct has attracted more and more attention not only because of its practical importance in various industrial applications, but also because of physically interesting phenomena under the action of centrifugal force caused by curvature of the pipe. Excellent surveys have been given by [3–6].

When a pipe rotates about an axis normal to a plane including the pipe, the Coriolis force could also contribute to the generation of secondary flow and the heat transfer becomes more complicated. Such rotating pipes have extensive applications, such as the cooling systems for conductors of electric generator motors, gas turbines, separation processes. The nature of the flow and heat transfer in rotating pipes is affected by the interaction of the imposed pressure-driven axial flow, the system rotation and the geometrical structure of the pipe. This interaction causes the fluid flow and heat transfer performance in a rotating pipe to be drastically different from those in a stationary case.

As an interesting problem, the combined effects of curvature and rotation, which are relevant to the flow in rotating curved pipes, were examined detailedly by numerous researchers [7–19]. Although the flow and heat transfer in the rotating curved pipes have been well studied, the helical pipes with rotation still receive relatively scant attention. To enhance the heat and mass transfer, the helical pipes with a finite pitch were used extensively in various industrial applications. Important characteristics include, in addition to high heat and mass transfer rate, enhanced cross-sectional mixing, low axial dispersion and an extended laminar flow. The previous works on the helical pipes were mainly focused on the stationary case, such as [20–24]. By the author's knowledge, no paper was published in the open literature for both theoretically and numerically studying the convective heat transfer in a rotating helical pipe.

* Corresponding author. Tel.: +86-571-87984209/87931869; fax: +86-571-87951464.
E-mail address: mec_zbzq@emb.zju.edu.cn (H. Chen).

0017-9310/$ - see front matter © 2003 Elsevier Ltd. All rights reserved.
doi:10.1016/S0017-9310(03)00350-8

Nomenclature

d	diameter of the helical pipe
$\boldsymbol{e}_{r^{**}}$, $\boldsymbol{e}_z$, $\boldsymbol{e}_\psi$	unit base vectors of the cylindrical coordinate system
Dn	Dean number, $Dn = Re\kappa^{1/2}$
F	ratio of the Coriolis force to the centrifugal force, $F = 1/\kappa Ro$
K	pitch of the helical pipe
Nu	Nusselt number
p	pressure
P	modified pressure, $P = p - \Omega^2\rho(R - r\cos\theta)^2/2 - \Omega^2\rho(r\sin\beta\sin\theta)^2/2$
Pr	Prandtl number, $Pr = \upsilon/\alpha$
R	curvature radius
Re	Reynolds number, $Re = w_m d/\upsilon$
Ro	Rossby number, $Ro = w_m/\Omega d\cos\beta$
r	radial direction coordinates
s	axial direction coordinates
$\boldsymbol{T}, \boldsymbol{N}, \boldsymbol{B}$	tangent, normal and binormal unit vector of the helix
T, T_w	temperature of fluid and the wall
u, v, w	physical velocity components
$\boldsymbol{V}$	vector of velocity
w_m	mean value of axial velocity on the cross-section

Greek symbols

α	thermal diffusivity
β	the slope between the helix and the horizontal plane
υ	kinematic viscosity of fluid
κ	curvature
τ	torsion
Ω	rotating angular velocity
θ	angular coordinate
ρ	density of the fluid
ψ	stream function

Subscripts and superscripts

*	dimensionless variable
max	maximum value
–	average value

Our emphasis in this paper is placed on the coupled effects of curvature, torsion and rotation on the convective heat transfer. It is assumed that the fluid flow is steady, laminar, hydrodynamically and thermally fully developed, and, the wall heat flux and the peripheral wall temperature are both uniform. The fully developed convective heat transfer in a rotating helical pipe is examined by employing perturbation method and finite volume method. A wide range of parameters is covered in this work. Three important aspects of convective heat transfer will be studied in detail: temperature distribution, the distributions of peripheral Nusselt number and Nusselt number ratio.

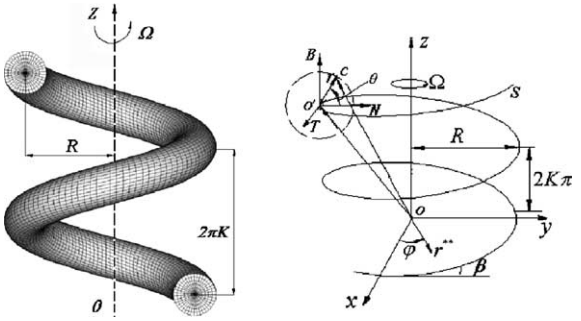

Fig. 1. The rotating helical and the rotating helical coordinate system.

2. The governing equations

Fig. 1 shows the rotating helical and the rotating helical coordinate system and the helix s, which is the centerline of the helical pipe, in a coordinate system (r^{**}, ψ, z). R is the radius of the helix and $2\pi K$ is the pitch. $\boldsymbol{e}_{r^{**}}$, $\boldsymbol{e}_z$, $\boldsymbol{e}_\psi$ are the unit base vectors of the cylindrical coordinate system. Then $ds = \sqrt{R^2 + K^2}\,d\theta$ and the curvature κ and torsion τ are obtained as

$$\kappa = \frac{R}{R^2 + K^2}, \quad \tau = \frac{K}{R^2 + K^2}$$

The radius vector of an arbitrary point o along the helix is expressed as

$$\boldsymbol{r}_o = R\boldsymbol{e}_{r^{**}}(\psi) + K\theta\boldsymbol{e}_z$$

The tangent unit vector $\boldsymbol{T}$, normal unit vector $\boldsymbol{N}$, and the binormal unit vector $\boldsymbol{B}$ of the helix are

$$\boldsymbol{T} = \boldsymbol{r}_o', \quad \boldsymbol{N} = \frac{1}{\kappa}\boldsymbol{r}_o'', \quad \boldsymbol{B} = \boldsymbol{T} \times \boldsymbol{N}$$

The Frenet formulas are

$$\boldsymbol{T}' = \kappa\boldsymbol{N}, \quad \boldsymbol{N}' = \tau\boldsymbol{B} - \kappa\boldsymbol{T}, \quad \boldsymbol{B}' = -\tau\boldsymbol{N}$$

And $\boldsymbol{T}$, $\boldsymbol{N}$, and $\boldsymbol{B}$ are given as

$$\boldsymbol{T}(s) = \cos\beta\boldsymbol{e}_\psi(s) + \sin\beta\boldsymbol{e}_Z$$
$$\boldsymbol{N}(s) = -\boldsymbol{e}_{r^{**}}(s)$$
$$\boldsymbol{B}(s) = -\sin\beta\boldsymbol{e}_\psi(s) + \cos\beta\boldsymbol{e}_z$$

where

$$\cos\beta = \frac{\kappa}{\sqrt{\kappa^2+\tau^2}}, \quad \sin\beta = \frac{\tau}{\sqrt{\kappa^2+\tau^2}}$$

A polar coordinate system (r,θ) in plane $(\boldsymbol{N},\boldsymbol{B})$ is defined, and radius vector $\boldsymbol{r}_c$ at an arbitrary point c is

$$\boldsymbol{r}_c(s) = \boldsymbol{r}_o(s) + r\cos\theta\boldsymbol{N}(s) + r\sin\theta\boldsymbol{B}(s)$$

Assume the helix s is rotating around OZ axial with a constant angular velocity Ω, or

$$\boldsymbol{\Omega} = \Omega\boldsymbol{e}_z$$

Accordingly, the Coriolis acceleration and the relative acceleration are

$$\begin{aligned}\boldsymbol{a}_c &= 2\boldsymbol{\Omega}\times\boldsymbol{V}\\ &= (2\Omega w\cos\beta - 2\Omega V_B\sin\beta)\boldsymbol{N} - 2\Omega U_N\cos\beta\boldsymbol{T}\\ &\quad + 2\Omega U_N\sin\beta\boldsymbol{B}\end{aligned}$$

$$\begin{aligned}\boldsymbol{a}_e &= \frac{\mathrm{d}\boldsymbol{\Omega}}{\mathrm{d}t}\times\boldsymbol{r}_c + \boldsymbol{\Omega}\times(\boldsymbol{\Omega}\times\boldsymbol{r}_c)\\ &= \Omega^2(R - r\cos\theta)\boldsymbol{N} + \frac{1}{2}\Omega^2 r\sin 2\beta\sin\theta\boldsymbol{T}\\ &\quad - \Omega^2 r\sin\theta\sin^2\beta\boldsymbol{B}\end{aligned}$$

where $U_N = u\cos\theta - v\sin\theta$, $V_B = u\sin\theta + v\cos\theta$, u, v, w are the physical velocity components of the radial, tangential and axial directions, respectively.

In terms of tensor analysis technique, assuming an incompressible, steady, and fully developed flow, the governing equations in (s,r,θ) (see Fig. 1) are

$$\frac{\partial u}{\partial r} + \frac{1}{r}\frac{\partial v}{\partial\theta} - \frac{\tau}{M}\frac{\partial w}{\partial\theta} + \left(\frac{1}{r} - \frac{\kappa\cos\theta}{M}\right)u + \frac{\kappa\sin\theta}{M}v = 0 \tag{1}$$

$$\begin{aligned}&u\frac{\partial u}{\partial r} + \frac{v}{r}\frac{\partial u}{\partial\theta} - \frac{\tau w}{M}\frac{\partial u}{\partial\theta} - \frac{v^2}{r} + \frac{\kappa\cos\theta}{M}w^2\\ &\quad = -\frac{\partial P}{\rho\partial r} - 2\Omega(w\cos\theta\cos\beta - v\sin\beta) + (\Delta V)^1\end{aligned} \tag{2}$$

$$\begin{aligned}&u\frac{\partial v}{\partial r} + \frac{v}{r}\frac{\partial v}{\partial\theta} - \frac{\tau w}{M}\frac{\partial v}{\partial\theta} + \frac{uv}{r} - \frac{\kappa\sin\theta}{M}w^2\\ &\quad = -\frac{1}{\rho r}\frac{\partial P}{\partial\theta} + 2\Omega(w\sin\theta\cos\beta - u\sin\beta) + (\Delta V)^2\end{aligned} \tag{3}$$

$$\begin{aligned}&u\frac{\partial w}{\partial r} + \frac{v}{r}\frac{\partial w}{\partial\theta} - \frac{\tau w}{M}\frac{\partial w}{\partial\theta} - \frac{\kappa\cos\theta}{M}uw + \frac{\kappa\sin\theta}{M}vw\\ &\quad = \frac{1}{\rho M}\left(\tau\frac{\partial P}{\partial\theta} - \frac{\partial P}{\partial s}\right) + 2\Omega(u\cos\theta - v\sin\theta) + (\Delta V)^3\end{aligned} \tag{4}$$

$$\begin{aligned}&u\frac{\partial T}{\partial r} + \frac{v}{r}\frac{\partial T}{\partial\theta} - \frac{\tau w}{M}\frac{\partial T}{\partial\theta} + \frac{w}{M}\frac{\partial T}{\partial s}\\ &\quad = \alpha\left[\frac{\partial^2 T}{\partial r^2} + \left(\frac{1}{r^2} + \frac{\tau^2}{M^2}\right)\frac{\partial^2 T}{\partial\theta^2} + \left(\frac{1}{r} - \frac{\kappa\cos\theta}{M}\right)\frac{\partial T}{\partial r}\right.\\ &\qquad \left. - \frac{k\sin\theta}{Mr}\frac{\partial T}{\partial\theta}\right]\end{aligned} \tag{5}$$

where $\frac{\partial P}{\partial s}$ and $\frac{\partial T}{\partial s}$ are the constants, and

$$\begin{aligned}(\Delta V)^1 &= \frac{\partial^2 u}{\partial r^2} + \left(\frac{1}{r^2} + \frac{\tau^2}{M^2}\right)\frac{\partial^2 u}{\partial\theta^2} + \left(\frac{1}{r} - \frac{\kappa\cos\theta}{M}\right)\frac{\partial u}{\partial r}\\ &\quad - \frac{A}{M^2}\frac{\partial u}{\partial\theta} - \frac{2}{r^2}\frac{\partial v}{\partial\theta} - \frac{2\kappa\tau\cos\theta}{M^2}\frac{\partial w}{\partial\theta}\\ &\quad - \left(\frac{1}{r^2} + \frac{\kappa^2\cos^2\theta}{M^2}\right)u + \frac{1}{M^2}\left(\kappa^2\sin\theta\cos\theta\right.\\ &\quad \left. - \frac{M\kappa\sin\theta}{r}\right)v + \frac{C}{M^2}w\end{aligned}$$

$$\begin{aligned}(\Delta V)^2 &= \frac{\partial^2 v}{\partial r^2} + \left(\frac{1}{r^2} + \frac{\tau^2}{M^2}\right)\frac{\partial^2 v}{\partial\theta^2} + \left(\frac{1}{r} - \frac{\kappa\cos\theta}{m}\right)\frac{\partial v}{\partial r}\\ &\quad - \frac{A}{M^2}\frac{\partial v}{\partial\theta} + \frac{2}{r^2}\frac{\partial u}{\partial\theta} + \frac{2\kappa\tau\sin\theta}{M^2}\frac{\partial w}{\partial\theta}\\ &\quad - \left(\frac{1}{r^2} + \frac{\kappa^2\sin^2\theta}{M^2}\right)v + \frac{1}{M^2}\left(\kappa^2\sin\theta\cos\theta\right.\\ &\quad \left. + \frac{M\kappa\sin\theta}{r}\right)v + \frac{D}{M^2}w\end{aligned}$$

$$\begin{aligned}(\Delta V)^3 &= \frac{\partial^2 w}{\partial r^2} + \left(\frac{1}{r^2} + \frac{\tau^2}{M^2}\right)\frac{\partial^2 w}{\partial\theta^2} + \left(\frac{1}{r} - \frac{\kappa\cos\theta}{m}\right)\frac{\partial w}{\partial r}\\ &\quad - \frac{A}{M^2}\frac{\partial w}{\partial\theta} + \frac{2\kappa\tau\cos\theta}{M^2}\frac{\partial u}{\partial\theta} - \frac{2\kappa\tau\sin\theta}{M^2}\frac{\partial v}{\partial\theta} - \frac{C}{M^2}u\\ &\quad - \frac{D}{M^2}v - \frac{\kappa^2}{M^2}w\end{aligned}$$

and

$$A = \frac{\kappa\tau^2 r}{M}\sin\theta - \frac{\kappa M}{r}\sin\theta$$

$$C = \frac{\kappa^2\tau r}{M}\sin\theta\cos\theta + \kappa\tau\sin\theta, \quad B = \frac{\kappa\tau r}{M}\sin\theta$$

$$D = -\frac{\kappa^2\tau r}{M}\sin^2\theta + \kappa\tau\cos\theta, \quad M = 1 - \kappa r\cos\theta$$

$$P = p - \frac{\Omega^2}{2}\rho(R - r\cos\theta)^2 - \frac{\Omega^2}{2}\rho(r\sin\beta\sin\theta)^2$$

Introduce the following dimensionless variables to obtain dimensionless equations,

$$s^* = \frac{s}{d}, \quad r^* = \frac{r}{d}, \quad w^* = \frac{w}{w_{\mathrm{m}}}, \quad u^* = \frac{ud}{\upsilon}$$

$$v^* = \frac{vd}{\upsilon}, \quad P^* = \frac{Pd^2}{\rho\upsilon^2}, \quad \kappa^* = \kappa d, \quad Dn = Re\sqrt{\kappa^*}$$

$$Re = \frac{w_{\mathrm{m}}d}{\upsilon}, \quad \tau^* = \tau d, \quad T^* = \frac{(T_{\mathrm{w}} - T)}{Prd\partial T/\partial s}, \quad Pr = \frac{\upsilon}{\alpha}$$

$$\Omega^* = \frac{\Omega d^2}{\upsilon}, \quad Ro = \frac{w_{\mathrm{m}}}{\Omega d\cos\beta}, \quad F = \frac{1}{\kappa Ro}$$

When $\Omega^* > 0$, the rotation has the same direction with the axial velocity (co-rotation), $\Omega^* < 0$ indicates the rotation and the axial velocity are in the opposite directions (counter-rotation).

The secondary stream function ψ is given as

$$\frac{1}{r}\frac{\partial\psi}{\partial\theta} = Mu, \quad -\frac{\partial\psi}{\partial r} = Mv - Gnrw \tag{6}$$

The boundary conditions:

$$\text{At } r = 1/2, \quad u = v = w = T = 0, \quad \frac{\partial\psi}{\partial r} = 0 \tag{7}$$

3. Perturbation solutions for small Dean number

For a small Dean number, Eqs. (1)–(5) can be solved by the perturbation method. Assuming $\frac{\kappa}{2} = \varepsilon \ll 1$, $\frac{\tau}{2} = \lambda\varepsilon \ll 1$. Both of the curvature κ and torsion τ then can be used as perturbation parameters. The axial velocity w, the secondary stream function ψ and the temperature can be expressed as follows:

$$\begin{aligned} Rew &= 2(\hat{w}_0(\hat{r},\theta) + \varepsilon\hat{w}_1(\hat{r},\theta) + \varepsilon^2\hat{w}_2(\hat{r},\theta) + \cdots) \\ \psi &= \varepsilon\hat{\psi}_1(\hat{r},\theta) + \varepsilon^2\hat{\psi}_2(\hat{r},\theta) + \cdots \\ T &= \hat{T}_0(\hat{r},\theta) + \varepsilon\hat{T}_1(\hat{r},\theta) + \varepsilon^2\hat{T}_2(\hat{r},\theta) + \cdots \end{aligned} \tag{8}$$

where $\hat{r} = 2r$. Substituting Eqs. (6) and (8) into the governing equations (1)–(5), and collecting the coefficient of the same order of ε, one can obtain the three sets of partial differential equations. Solve the equations with the boundary conditions (7), one can get the second order solutions of the flow in a rotating helical circular pipe as

$$\hat{w}_0 = \frac{1}{4}(1-\hat{r}^2)\hat{G} \tag{9a}$$

$$\begin{aligned} \hat{\psi}_1 = {} & \left(\frac{1}{4608}\hat{r}^7\hat{G}^2 - \frac{1}{768}\hat{r}^5\hat{G}^2 - \frac{1}{192}\hat{r}^5\hat{G}\hat{\Omega} + \frac{1}{512}\hat{r}^3\hat{G}^2 \right. \\ & \left. + \frac{1}{96}\hat{r}^3\hat{G}\hat{\Omega} - \frac{1}{1152}\hat{r}\hat{G}^2 - \frac{1}{192}\hat{r}\hat{G}\hat{\Omega}\right)\sin\theta \\ & - \lambda\left(\frac{1}{16}\hat{r}^4\hat{G} + \frac{1}{8}\hat{r}^2\hat{G} - \frac{1}{16}\hat{G}\right) \end{aligned} \tag{9b}$$

$$\begin{aligned} \hat{w}_1 = {} & \left(-\frac{1}{737280}\hat{r}^9\hat{G}^3 + \frac{1}{73728}\hat{r}^7\hat{G}^3 \right. \\ & + \frac{1}{18432}\hat{r}^7\hat{G}^2\hat{\Omega} - \frac{1}{24576}\hat{r}^5\hat{G}^3 - \frac{1}{4608}\hat{r}^5\hat{G}^2\hat{\Omega} \\ & + \frac{1}{18432}\hat{r}^3\hat{G}^3 + \frac{1}{3072}\hat{r}^3\hat{G}^2\hat{\Omega} - \frac{3}{16}\hat{r}^3\hat{G} \\ & \left. - \frac{19}{737280}\hat{r}\hat{G}^3 - \frac{1}{6144}\hat{r}\hat{G}^2\hat{\Omega} + \frac{3}{16}\hat{r}\hat{G}\right)\cos\theta \end{aligned} \tag{9c}$$

$$\begin{aligned} \hat{\psi}_2 = {} & \left(-\frac{5}{442368}\hat{r}^5\lambda\hat{G}^3 - \frac{1}{18432}\hat{r}^5\lambda\hat{G}^2\hat{\Omega} - \frac{1}{24}\hat{r}^5\lambda\hat{G} \right. \\ & + \frac{1}{36864}\hat{r}^7\lambda\hat{G}^2\hat{\Omega} + \frac{1}{147456}\hat{r}^7\lambda\hat{G}^3 - \frac{1}{491520}\hat{r}^9\lambda\hat{G}^3 \\ & - \frac{1}{184320}\hat{r}^9\lambda\hat{G}^2\hat{\Omega} + \frac{1}{4423680}\hat{r}^{11}\lambda\hat{G}^3 \\ & - \frac{13}{4423680}\hat{r}\hat{G}^3\lambda - \frac{1}{61440}\hat{r}\hat{G}^2\hat{\Omega}\lambda - \frac{1}{24}\hat{r}\lambda\hat{G} \\ & \left. + \frac{41}{4423680}\hat{r}^3\hat{G}^3\lambda + \frac{1}{20480}\hat{r}^3\hat{G}^2\hat{\Omega}\lambda + \frac{1}{12}\hat{r}^3\lambda\hat{G}\right)\cos\theta \\ & + \left(\frac{1}{11890851840}\hat{G}^4\hat{r}^{14} + \frac{1}{512}\hat{G}\hat{r}^6\hat{\Omega} \right. \\ & - \frac{1}{412876800}\hat{G}^4\hat{r}^{12} - \frac{1}{103219200}\hat{G}^3\hat{r}^{12}\hat{\Omega} \\ & - \frac{1}{8847360}\hat{G}^2\hat{r}^{10}\hat{\Omega} + \frac{1}{56623104}\hat{G}^4\hat{r}^{10} \\ & - \frac{1}{2211840}\hat{G}^3\hat{r}^8\hat{\Omega} - \frac{1}{13271040}\hat{G}^4\hat{r}^8 \\ & + \frac{13}{15360}\hat{r}^4\hat{G}^2 + \frac{7}{46080}\hat{r}^8\hat{G}^2 + \frac{11}{7077888}\hat{G}^3\hat{r}^6\hat{\Omega} \\ & + \frac{1}{442368}\hat{G}^2\hat{r}^6\hat{\Omega}^2 + \frac{1}{13271040}\hat{G}^3\hat{r}^{10}\hat{\Omega} \\ & + \frac{1037}{1238630400}\hat{G}^3\hat{r}^2\hat{\Omega} + \frac{1}{5242880}\hat{G}^4\hat{r}^6 \\ & - \frac{85}{396361728}\hat{G}^4\hat{r}^4 - \frac{1}{245760}\hat{G}^2\hat{r}^4\hat{\Omega}^2 \\ & + \frac{4979}{59454259200}\hat{G}^4\hat{r}^2 - \frac{149}{74317824}\hat{G}^3\hat{r}^4\hat{\Omega} \\ & - \frac{1}{256}\hat{r}^4\hat{G}\hat{\Omega} - \frac{1}{1536}\hat{G}^2\hat{r}^6 + \frac{17}{8847360}\hat{G}^2\hat{r}^2\hat{\Omega} \\ & \left. - \frac{1}{2880}\hat{r}^2\hat{G}^2 + \frac{1}{512}\hat{r}^2\hat{G}\hat{\Omega}\right)\sin\theta\cos\theta \end{aligned} \tag{9d}$$

$$\begin{aligned} w_2 = {} & \lambda\sin\theta\left(\sum_{i=0}^{1}\sum_{j=1}^{7}A_{ij}\hat{r}^{2j-1-i}\hat{G}^{4-i}\hat{\Omega}^i + \hat{G}\sum_{j=1}^{4}A_j^1\hat{r}^j\right) \\ & + \cos 2\theta\sum_{i=0}^{2}\sum_{j=1}^{3}\sum_{k=1}^{6-i+j}B_{ijk}^{(1)}\hat{r}^{2k}\hat{G}^{2j-i-1}\hat{\Omega}^i \\ & + \sum_{i=0}^{2}\sum_{j=1}^{2}\sum_{k=0}^{6-i+j}B_{ijk}^{(2)}\hat{r}^{2k}\hat{G}^{2j-i+1}\hat{\Omega}^i \end{aligned} \tag{9e}$$

where $\hat{G} = -\frac{1}{8}\frac{\partial P}{\partial s}$, $\hat{\Omega} = \frac{FRe}{2}$ and the coefficients A_{ij}, A_j^1, $B_{ijk}^{(1)}$, $B_{ijk}^{(2)}$ are integral constants. And finally, the zero-, first-, and second-order temperature are derived as

$$\hat{T}_0 = \frac{1}{128}\hat{r}^4\hat{G} - \frac{1}{32}\hat{G}\hat{r}^2 + \frac{3}{128}\hat{G} \tag{10a}$$

$$\hat{T}_1 = \left(\frac{1}{8\,847\,360}\hat{r}^{11}\hat{G}^3 Pr - \frac{1}{1\,474\,560}\hat{r}^9\hat{G}^2\hat{\Omega} + \frac{1}{221\,184}\hat{r}^7\hat{G}^2\hat{\Omega} - \frac{1}{73\,728}\hat{r}^5\hat{G}^2\hat{\Omega} - \frac{1}{737\,280}\hat{r}^9\hat{G}^3 Pr + \frac{7}{1\,179\,648}\hat{r}^7\hat{G}^3 Pr + \frac{1}{49\,152}\hat{r}^3\hat{G}^2\hat{\Omega} - \frac{11}{884\,736}\hat{G}^3\hat{r}^5 Pr + \frac{1}{73\,728}\hat{G}^3\hat{r}^3 Pr + \frac{1}{48}\hat{r}^5\hat{G} + \frac{1}{88\,473\,600}\hat{r}^{11}\hat{G}^3 - \frac{73}{44\,236\,800}\hat{r}\hat{G}^3 + \frac{19}{5\,898\,240}\hat{r}^3\hat{G}^3 + \frac{1}{1\,179\,648}\hat{r}^7\hat{G}^3 - \frac{103}{17\,694\,720}\hat{G}^3\hat{r}Pr - \frac{47}{4\,423\,680}\hat{r}\hat{G}^2\hat{\Omega} + \frac{1}{12\,288}\hat{G}^2\hat{r}^3\hat{\Omega}Pr - \frac{1}{245\,760}\hat{r}^9\hat{G}^2\hat{\Omega}Pr + \frac{1}{36\,864}\hat{r}^7\hat{G}^2\hat{\Omega}Pr - \frac{5}{73\,728}\hat{G}^2\hat{r}^5\hat{\Omega}Pr + \frac{19}{384}\hat{r}\hat{G} - \frac{9}{128}\hat{r}^3\hat{G} - \frac{1}{442\,368}\hat{r}^5\hat{G}^3 - \frac{1}{5\,898\,240}\hat{r}^9\hat{G}^3 - \frac{3}{81\,920}\hat{r}\hat{G}^2\hat{\Omega}Pr \right) \frac{\cos\theta}{2} \tag{10b}$$

$$\hat{T}_2 = \lambda \sin\theta \left(\sum_{i=0}^{1}\sum_{j=0}^{2}\sum_{k=1}^{7-i} C_{ijk}\hat{r}^{2k+1}\hat{G}^{4-i}Pr^j\hat{\Omega}^i + \hat{G}^2\sum_{i=0}^{1}\sum_{j=1}^{4} D_{ij}\hat{r}^{2j+1}Pr^i \right) + \cos(2\theta) \times \sum_{i=0}^{2}\sum_{j=1}^{2}\sum_{k=1}^{8-i+j}\sum_{m=0}^{2} E_{ijk}^{(m)}\hat{r}^{2k}\hat{G}^{2j-i+1}\hat{\Omega}^i Pr^m + \sum_{i=0}^{2}\sum_{j=1}^{2}\sum_{k=0}^{8-i+j}\sum_{m=0}^{2} F_{ijk}^{(m)}\hat{r}^{2k+1}\hat{G}^{3j-i-1}\hat{\Omega}^i Pr^m \tag{10c}$$

where C_{ijk}, D_{ij}, $E_{ijk}^{(m)}$, $F_{ijk}^{(n)}$, E_i are the integral constants.

4. Numerical procedure

In present work, the finite-volume method is chosen to solve the governing equations. The power-law scheme is adopted to discretize the convection term and the SIMPLE scheme is employed to deal with the problem of velocity–pressure coupling. The mesh system is staggered and an alternating direction line by line iterative method (ADI) with block correction technique is used to solve the discretized equations. The description of the numerical implementation can be found, for example from Patankar's work [25].

For a given Dn, an iterative procedure should be applied to obtain a specific value of axial pressure gradient $-\partial P/\partial s$. A value of $-\partial P/\partial s$ is first guessed and the obtained flow rate is compared with the given flow rate. If the former is smaller (or larger) than the latter, we should increase (or decrease) $-\partial P/\partial s$ until the two flow rates almost reach a same value. The convergence criterion is $|(\phi^{n+1} - \phi^n)/\phi^n| < 10^{-7}$.

A uniform grid mesh system is employed in the whole cross-section because the boundary layers exist not only near the wall but also at the dividing boundary of the secondary flow. Four pairs of grid sizes ($r \times \theta = M \times N$) were used to check the grid dependence, and associated comparisons are shown in the Table 1. 22×42 is chosen as reasonable grid size for the flow in rotating helical circular pipes. For a high Dean number ($Dn \geqslant 500$), 32×62 is employed to satisfy precision.

Table 1
Grid test ($Dn = 100$, $\kappa = 0.1$, $\tau = 0.1$)

F	Grid	λRe	T_{max}	$\overline{Nu}/\overline{Nu}_s$
0	12×32	22.2092	17.6438	1.6176
	22×42	22.0528	18.3333	1.5793
	22×62	22.0544	18.3352	1.5792
	32×62	22.0559	18.3899	1.5753
5	12×32	31.5932	13.9567	2.3349
	22×42	31.0669	14.6506	2.1572
	32×62	31.0657	14.6581	2.1558
	32×62	31.0518	14.6789	2.1544
−5	12×32	28.7410	15.8314	2.0435
	22×42	28.3097	16.1975	1.9431
	22×62	28.3105	16.1999	1.9411
	32×62	28.2593	16.2144	1.9516

For the rotating cases, comparisons are made with the available results [12]. The Nusselt number ratio obtained by present numerical method as well as available results are shown in Fig. 2. For the small Dean number ($Dn = 100$), the numerical curves almost has very good agreement with that of Ishigaki [12], but for a large Dean number ($Dn = 500$), their differences become significant, perhaps Ishigaki [12] did not take the effect of high order terms of curvature into account. Meanwhile, some comparisons between the numerical solution and the perturbation solution are also made and two solutions confirm each other very well.

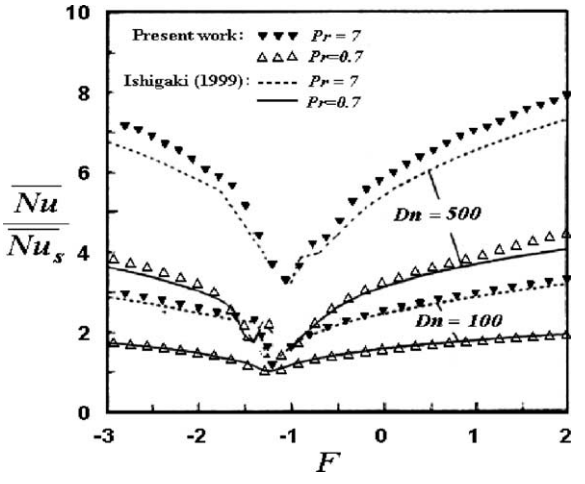

Fig. 2. Comparison with available results ($\kappa = 0.02$).

5. Results and discussions

In a rotating helical pipe, the presence of centrifugal and Coriolis forces cause two kinds of secondary flows in the cross-section perpendicular to the axial velocity. The interaction of these two secondary flows will make the heat transfer performance drastically different from those in a stationary case. Our work focuses on the convective heat transfer in a rotating helical pipe and the results shown in the paper will be confined to the case of $Pr = 0.7$.

5.1. Temperature distribution from the perturbation solutions

Fig. 3 presents the distributions of different order solutions of temperature. In the temperature contours, solid, dotted and dot-dash lines indicate positive, zero, and negative values respectively. Eq. (10b) indicates that the torsion has no effect on $\hat{T}_1\kappa$ and as is seen in Fig. 3(a), the distributions of $\hat{T}_1\kappa$ is symmetrical to the center line. For the co-rotation ($F = 1$) and stationary case ($F = 0$), $\hat{T}_1\kappa$ has a positive value in the semicircle near the outer wall and a negative value near the inner bend, obviously, the maximum temperature is pushed to outer bend. When $F = -1.2$, a negative value region appears in the outer half while a positive value region appears near the inner wall. And the maximum of $\hat{T}_1\kappa$ becomes small, so the effect of $\hat{T}_1\kappa$ on temperature becomes weakest. As F decreases to -2, the distribution of $\hat{T}_1\kappa$ behaves almost in the same structure as those in the case of $F = 0$, but a reverse way.

The torsion affects the distribution of $\hat{T}_2\kappa^2$, as seen in Fig. 3(b). For $F = 1$ and 0, the contours of $\hat{T}_2\kappa^2$ are highly asymmetrical with a negative value in the bottom region and a positive value in the upper region. These distributions will shift the maximums of the temperature to the upper half. But for the counter-rotation $F = -2$, the contour of $\hat{T}_2\kappa^2$ behaves the reverse way and when $F = -1.2$, the effect of $\hat{T}_2\kappa^2$ on T can almost be neglected. By combining $\hat{T}_0$, $\hat{T}_1\kappa$ and $\hat{T}_2\kappa^2$, Fig. 3(c) shows the variations of typical temperature distribution with F. As F decreases from 1 to -2, the maximum of temperature shifts form the upper-outer half to the lower-inner half and it seems to rotate clockwise.

5.2. Temperature distribution from the numerical procedure

Fig. 4 shows the variations of temperature distributions with F for a large Dn number. In this case, the effect of centrifugal force on the temperature distribution becomes more evident and the temperature distribution is not similar to concentric circles. For the co-rotation ($F = 1$), the high temperature is pushed to the outer wall.

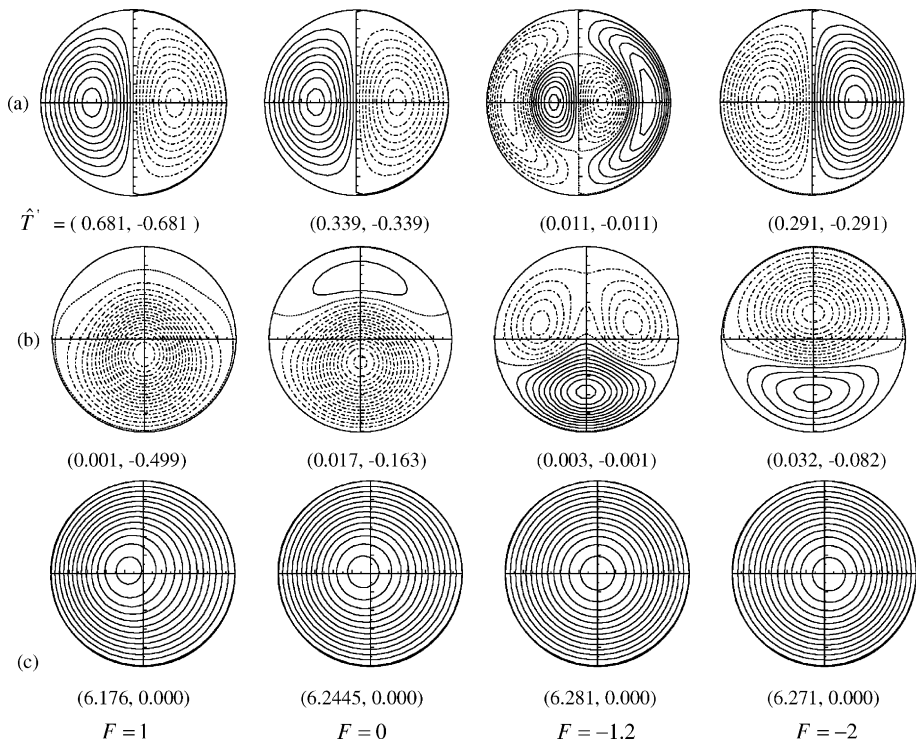

Fig. 3. Temperature distribution of $\hat{T}_1\kappa$, $\hat{T}_2\kappa^2$ and T ($Dn = 15$, $\kappa = 0.05$, $\tau = 0.1$, $\hat{T}' = (\text{maximum}, \text{minimum})$; (a) $\hat{T}_1\kappa$, (b) $\hat{T}_2\kappa^2$, (c) T, $T = \hat{T}_0 + \hat{T}_1\kappa + \hat{T}_2\kappa^2$).

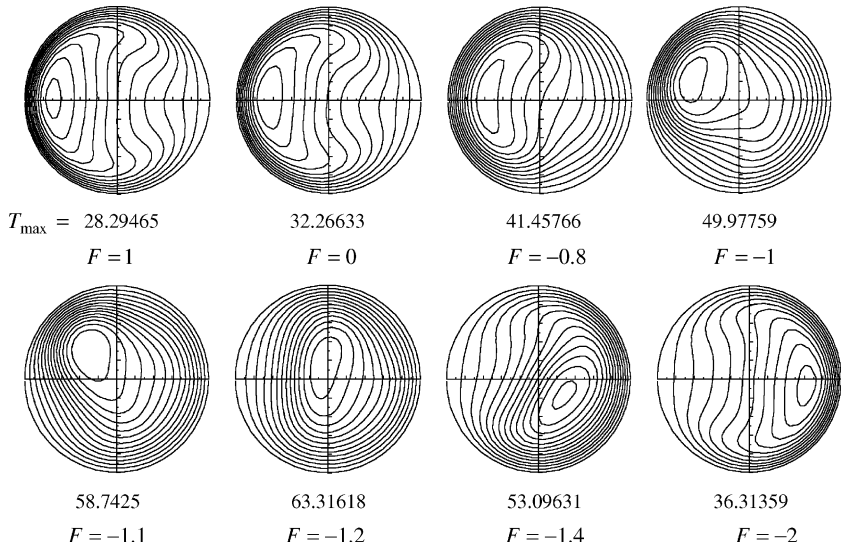

Fig. 4. Variations of temperature distributions with F ($Dn = 250$, $\kappa = 0.1$, $\tau = 0.1$).

For the counter-rotation ($F < 0$), the opposite Coriolis force will dominate the temperature distribution gradually as F decreases from 0 to -2. When $F = -2$, the temperature distribution dominated by the reversal Coriolis force can be recognized. Fig. 4 also indicates that for a large Dn number, Only when the Corioslis force almost has the same magnitude with the centrifugal force but in the opposite direction ($F \approx -1$), the effect of torsion on temperature is remarkable.

Fig. 5 shows the variations of T_{max} with F. The figure indicates that when $F \approx -1.2$, T_{max} reaches its maximum values for different values of Dn, which means the maximum temperature difference between flow and wall becomes largest in this point. These phenomena can be well understood if we realise that when $F \approx -1.2$, the secondary flows caused by the centrifugal and Coriolis forces almost counteract with each other and the mixing by secondary flow becomes weakest. For a given F, the larger Dn number, the larger T_{max}.

Most of the existing studies on curved rotating pipe are almost on the small curvature and torsion, such as Ishigaki [15,16] and Zhang and Zhang [24]. In engineering applications, a large curvature is often encountered and it is important and interesting to study the effects of curvature on the flow. Fig. 6 provides the variations of the maximum temperature difference T_{max} with κ for different values of F. As κ increases, the secondary flow is intensified by the centrifugal force and the temperature difference is reduced because of the remarkable mixing by secondary flow. Fig. 7 shows the

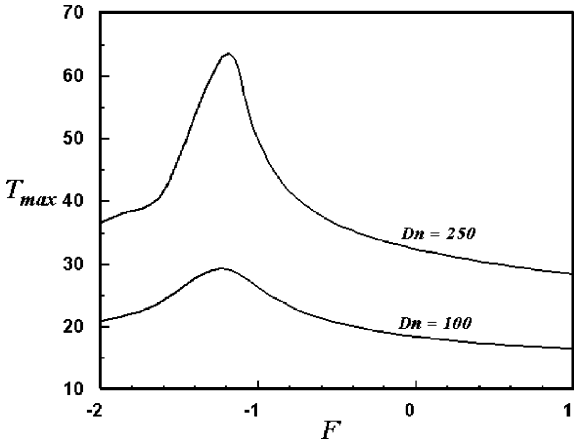

Fig. 5. Variations of T_{max} with F for different values of Dn ($\kappa = 0.1$, $\tau = 0.1$).

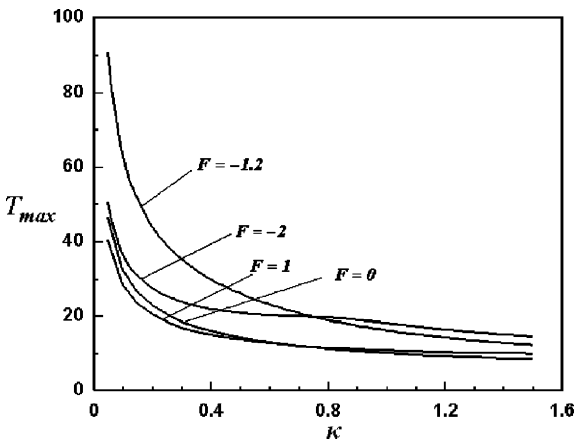

Fig. 6. Variations of T_{max} with κ for different values of F ($Dn = 250$, $\tau = 0$).

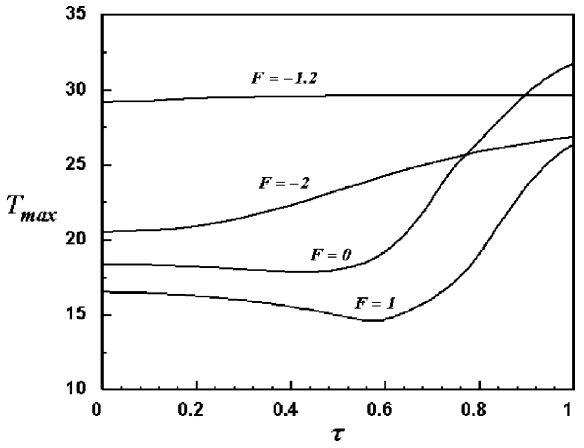

Fig. 7. Variations of $T_{\max}$ with τ for different values of F ($Dn = 250$, $k = 0.1$).

variations of $T_{\max}$ with τ. The effect of torsion on $T_{\max}$-curves changes with F. For $F = 0$ and 1, $T_{\max}$ first decreases and then increases with increasing torsion while for $F = -2$, $T_{\max}$ increases with increasing torsion all along. When $F = -1.2$, increasing torsion almost has no effect on $T_{\max}$.

5.3. Nusselt number

The non-dimensional peripheral Nusselt is defined as

$$Nu = \frac{2}{T_b}\left(\frac{\partial T}{\partial r}\right)_{r=0.5} \tag{11}$$

where T_b is the bulk temperature, $T_b = \int_0^{0.5}\int_0^{2\pi} Twr \times dr\,d\theta / \int_0^{0.5}\int_0^{2\pi} wr\,dr\,d\theta$.

The variations of Nu along the wall circumference are shown by polar diagrams in Fig. 8. As κ increases, the distribution of Nu is distorted gradually and the Nu-curves seems to be pushed to the inner bend and the outer bend at the same time. When $\kappa = 1.5$, for $F = -1.2$ and -2, two Nu maximum appears. As τ increases, the Nu-curve rotates clockwise for $F = 1$ and -2. But for $F = -1.2$, increasing τ has little influence on

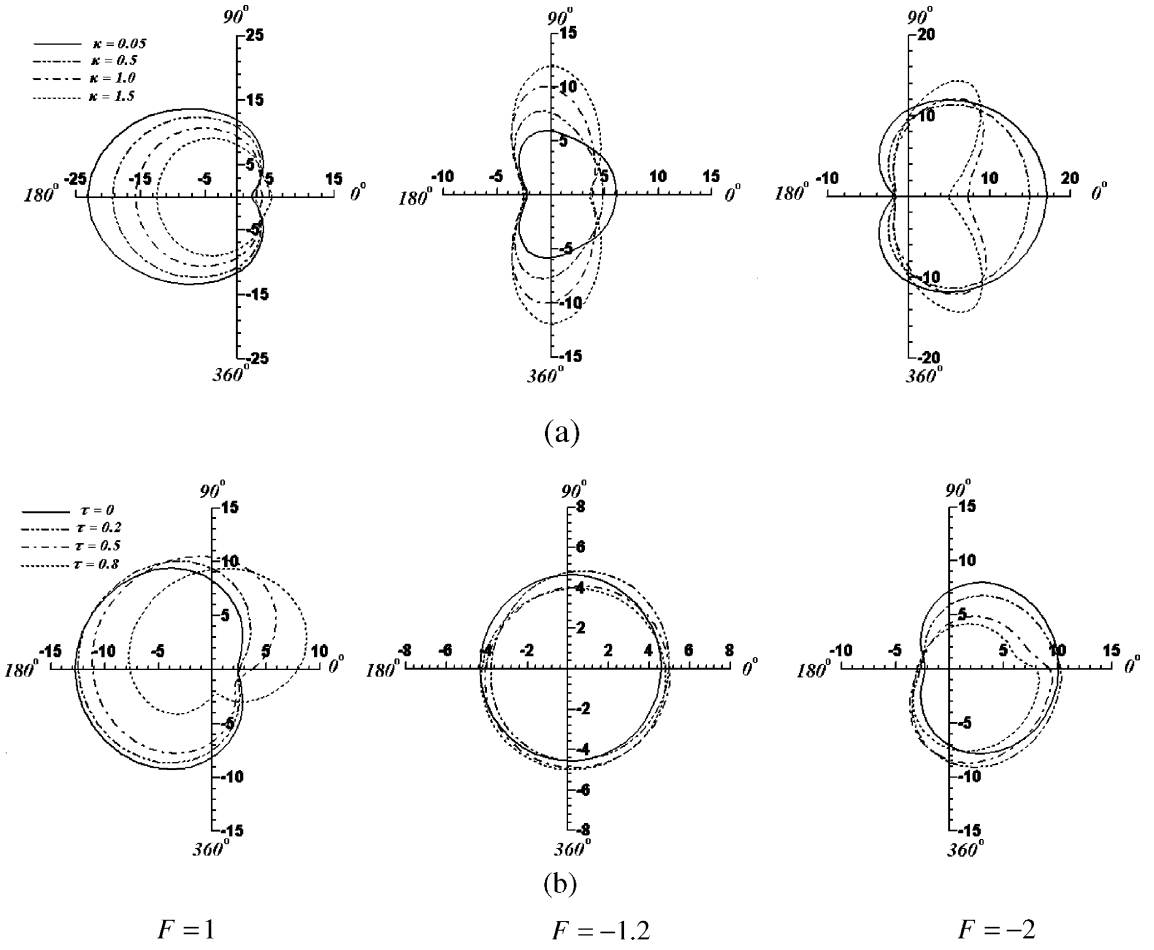

Fig. 8. Nusselt number distributions along the wall. (a) $Dn = 250$, $\tau = 0$ and (b) $Dn = 100$, $\kappa = 0.1$.

Nu distribution. Considering *Nu* is proportional to the temperature jumped from wall, all the above variations can be explained by the distributions of the temperature distribution.

By integrating Eq. (11) along the peripheral of pipe, the expression of average Nusselt number for the small parameter can also be obtained as

$$\begin{aligned}\overline{Nu} &= \frac{1}{2\pi}\int_0^{2\pi}\frac{2}{T_b}\left(\frac{\partial T}{\partial r}\right)_{r=1}\mathrm{d}\theta \\ &= \left(\left(\frac{5}{64}\hat{G} - \frac{3}{20\,480}\hat{G}^2\hat{\Omega} - \frac{1}{2304}\hat{G}\hat{\Omega}^2 \right.\right. \\ &\quad - \frac{1}{23\,040}\hat{G}^2\hat{\Omega}Pr - \frac{11}{884\,736}\hat{G}^3 - \frac{29}{4\,423\,680}\hat{G}^3Pr \\ &\quad - \frac{1}{60\,660\,288}\hat{G}^3\hat{\Omega}^2 - \frac{37}{7\,927\,234\,560}\hat{G}^4\hat{\Omega} \\ &\quad \left.\left. - \frac{1541}{428\,070\,662\,400}\hat{G}^5\right) + \frac{1}{4}\hat{G}\right)\Big/ T_b \end{aligned} \tag{12}$$

Fig. 9 shows the variation of $\overline{Nu}/\overline{Nu}_s$ with F. In the Fig. 9(a), the perturbation results agree well with the numerical results when $Dn = 10$ and 15. But for $Dn = 20$, the difference between perturbation results and

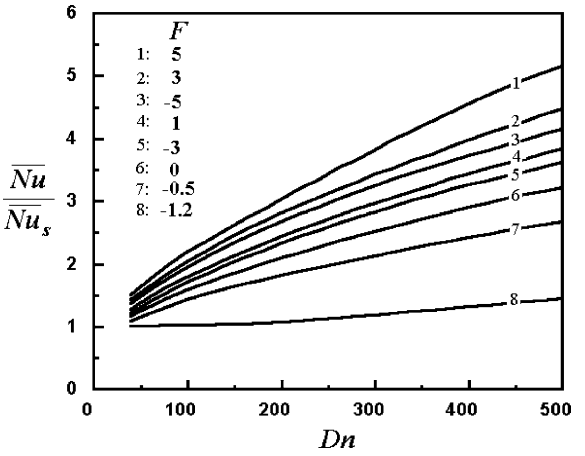

Fig. 10. Variation of Nusselt number ratio with Dn ($\kappa = 0.1$, $\tau = 0.1$).

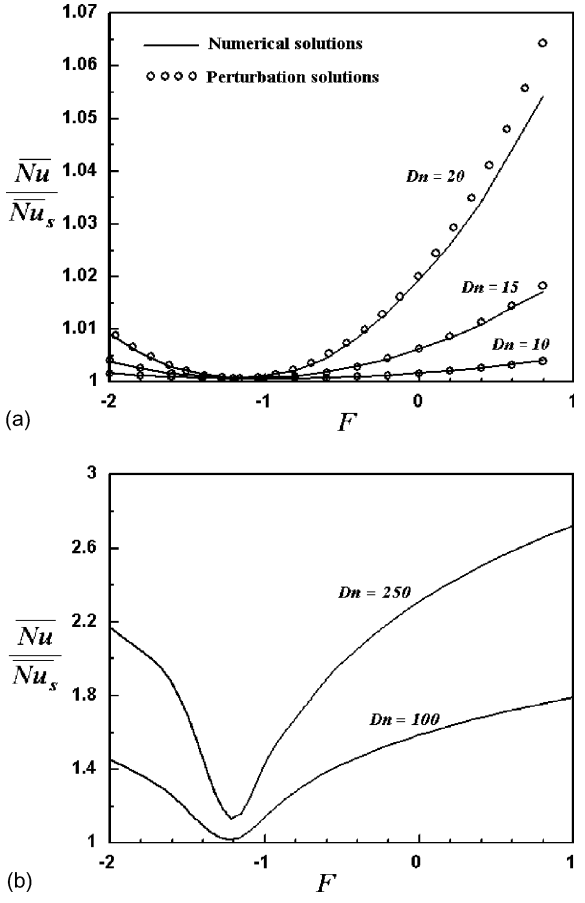

Fig. 9. Variation of Nusselt number ratio with F ((a) $\kappa = 0.05$, $\tau = 0.1$, (b) $\kappa = 0.1$, $\tau = 0.1$).

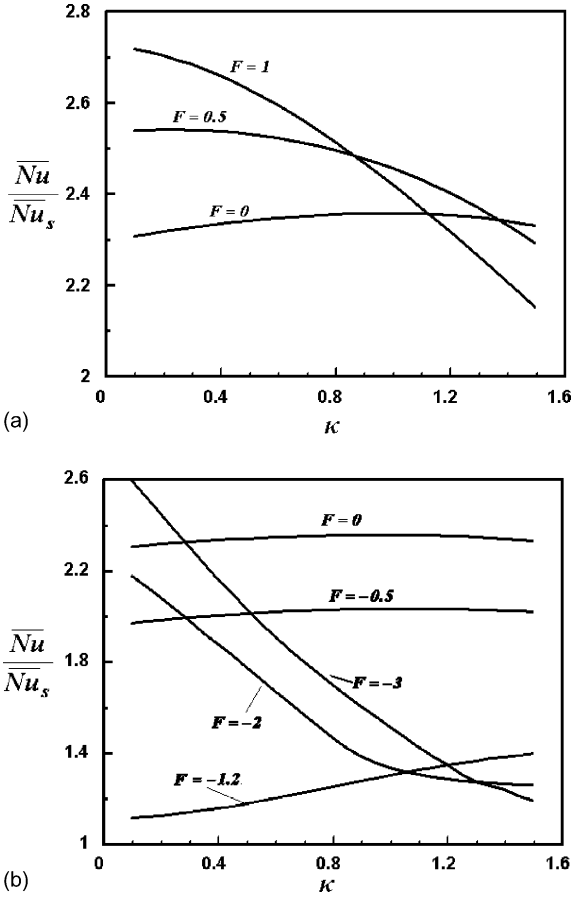

Fig. 11. Variation of Nusselt number ratio with κ ($Dn = 250$, $\tau = 0$).

the numerical results becomes more obvious as F increases. All of the $\overline{Nu}/\overline{Nu}_s$-curves reach their minimum values about 1 when $F \approx -1.2$, which indicates the Nusselt number in this point almost has the same value with straight pipe. When $F > -1.2$, $\overline{Nu}/\overline{Nu}_s$ increases as F increases, when $F < -1.2$, $\overline{Nu}/\overline{Nu}_s$ decreases as F increases. The similar variations also can be found for a large Dn, see in Fig. 9(b). Fig. 10 shows some numerical results for a wide range of Dn number. For all the value of F, the $\overline{Nu}/\overline{Nu}_s$-curves increase as Dn increases.

The variation of $\overline{Nu}/\overline{Nu}_s$ with κ is shown in Fig. 11. For the stationary case ($F = 0$), the $\overline{Nu}/\overline{Nu}_s$-curves first increase with increasing κ until at a certain value of κ and then decrease as κ increases. For the co-rotation ($F = 1$, 0.5), the $\overline{Nu}/\overline{Nu}_s$-curves decrease as κ increases. However, for the counter-rotation, the variation of $\overline{Nu}/\overline{Nu}_s$-curves depends on F. For $F = -1.2$, the $\overline{Nu}/\overline{Nu}_s$-curves increase with increasing κ while for $F = -2$ and -3, the $\overline{Nu}/\overline{Nu}_s$-curves decrease with increasing κ.

Fig. 12 presents the variation of $\overline{Nu}/\overline{Nu}_s$ with τ. For the co-rotation cases ($F = 1$, 0.5), $\overline{Nu}/\overline{Nu}_s$ slightly increases with increasing τ and reach its maximum values at $\tau \approx 0.5$, then it decreases obviously as τ increases. For the counter-rotation, all of the $\overline{Nu}/\overline{Nu}_s$-curves almost decrease as τ decreases. Fig. 12 also indicates that when $F \approx -1.2$, increasing τ has little effect on $\overline{Nu}/\overline{Nu}_s$ and $\overline{Nu}/\overline{Nu}_s$ almost keeps constant all the way with increasing τ.

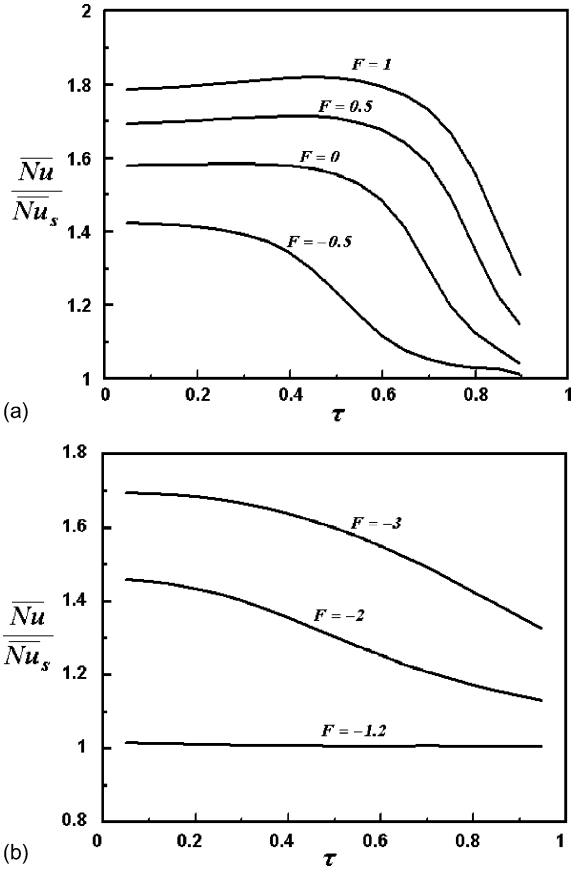

Fig. 12. Variation of Nusselt number ratio with τ ($Dn = 100$, $\tau = 0.1$).

6. Conclusions

The convective heat transfer in the rotating helical pipes with arbitrary curvature and torsion are investigated by perturbation and finite volume methods. The coupled effects of rotation, curvature, and torsion on the convective heat transfer in the rotating helical pipes are first examined in details. The major conclusions are drawn as follows:

The effect of torsion on the temperature distributions occurs only in the second-order solution. For counter-rotation, increasing curvature can divide the high region into two regions. Whether the high temperature is near the inner bend or the outer bend depends on the value of F. Increasing curvature and torsion will also affect the convective heat transfer in rotating helical pipes significantly. Only there are effects of the curvature or the rotation on the temperature distribution, the effects of torsion can be recognized.

The distribution of Nu along the wall is dependent on the distribution of temperature. The Nusselt number ratio increases for co-rotation with F increasing, but for counter-rotation, first decreases and reaches its minimum about 1 at $F \approx -1$. Whether increasing τ or κ increases the heat transfer ratio or decreases it depends on the value of F.

Acknowledgements

The authors wish to thank the financial support of the National Natural Science Foundation of P.R. China (Grant no.: 10272096).

References

[1] W.R. Dean, Note on the motion of fluid in a curved pipe, Phil. Mag. 7 (4) (1927) 208–223.
[2] W.R. Dean, The stream-line motion of fluid in a curved pipe, Phil. Mag. 7 (5) (1928) 673–695.
[3] S.A. Berger, L. Talbot, L.S. Yao, Flow in a curved pipe, Ann. Rev. Fluid Mech. 15 (1983) 410–512.
[4] K. Nandakumar, J.H. Masiyah, Swirling flow and heat transfer in oiled and twisted pipe, in: A.S. Mujumdar, R.A. Mashelkar (Eds.), Advances in Transport Processes, vol. 4, Wiley, 1986, pp. 49–112.
[5] H. Ito, Flow in curved pipe, Jpn. Soc. Mech. Engng. Int. J. 30 (1987) 543–552.

[6] S.A. Berger, Flow and heat transfer in curved pipes and tubes, AIAA Paper (1991) 91-0030.
[7] H. Ludwieg, Die Ausgebildete Kanalströmung in einem rotierenden system, Ingenieur-archiv 19 (1951) 296–308.
[8] H. Miyazaki, Combined free and force convective heat transfer and fluid flow in rotating curved circular tube, Intl. J. Heat Mass Transfer 14 (1971) 1295–1309.
[9] H. Miyazaki, Combined free and forced convective heat transfer and fluid flow in a rotating curved rectangular tube, Trans. ASME C: J. Heat Transfer 95 (1973) 64–71.
[10] H. Ito, T. Motai, Secondary flow in a rotating curved pipe, Rep. Inst. High Speed Mech. 29 (1974) 33–57.
[11] H. Ito, H. Aakita, S. Hasegawa, M. Suzuki, Numerical and experimental study on laminar flow in a rotating curved pipe (1. constant Dean number), Mem. Inst. High Speed Mech. 58 (1987) 185–235.
[12] H. Ito, H. Aakita, S. Hasegawa, M. Suzuki, Numerical and experimental study on laminar flow in a rotating curved pipe (2. constant rotational Reynolds number), Mem. Inst. High Speed Mech. 59 (1988) 45–96.
[13] P. Daskopoulos, A.M. Lenhoff, Flow in curved ducts. Part 2. Rotating ducts, J. Fluid Mech. 217 (1990) 575–593.
[14] M. Selmi, K. Nandakumar, W.H. Finlay, A bifurcation study viscous flow through a rotating curved duct, J. Fluid Mech. 262 (1994) 353–375.
[15] H. Ishigaki, Laminar flow in rotating curved pipes, J. Fluid Mech. 329 (1996) 373–388.
[16] H. Ishigaki, Laminar convective heat transfer in rotating curved pipes, JSME Int. J. 42, Ser. B (1999) 489–497.
[17] K. Yamamoto, S. Yanae, M.M. Alam, Flow through a rotating curved duct with square cross-section, J. Phys. Soc. Jpn. 68 (1999) 1173–1184.
[18] J.S. Zhang, B.Z. Zhang, J.W. Jü, Fluid flow in rotating curved rectangular duct, Int. J. Heat Fluid Flow 22 (2001) 583–592.
[19] J.S. Zhang, X.R. Shen, B.Z. Zhang, The Flow in rotating curved pipe, J. Hydrodyn. 12, Ser. B (1) (2000) 108–116.
[20] M. Germano, On the effect of torsion on a helical pipe flow, J. Fluid Mech. 125 (1982) 1–8.
[21] E.R. Tuttle, Laminar flow in twisted pipes, J. Fluid Mech. 219 (1990) 545–570.
[22] S. Liu, J.H. Masliyah, Axially invariant laminar flow in helical pipes with a finite pitch, J. Fluid Mech. 251 (1993) 315–353.
[23] L. Zabielski, A.J. Mestel, Steady flow in a helically symmetric pipe, J. Fluid Mech. 370 (1998) 297–320.
[24] J.S. Zhang, B.Z. Zhang, Flow in a helical pipe, ACTA Mech. Sinica 15 (4) (1999) 298–312.
[25] S.V. Patankar, Numerical Heat Transfer and Fluid Flow, McGraw-Hill, 1980.